Controlling liquid landscape with 3D-printed spines: A tool for micromanipulation

Megan Delens (megan.delens@uliege.be)
University of Liege https://orcid.org/0000-0002-7180-9451
Axel Franckart
University of Liege
Nicolas Vandewalle
University of Liege

Article

Keywords:

Posted Date: October 20th, 2023

DOI: https://doi.org/10.21203/rs.3.rs-3467162/v1

Additional Declarations: There is **NO** Competing Interest.

Controlling liquid landscape with 3D-printed spines: A tool for micromanipulation

M.Delens,* A.Franckart, and N.Vandewalle
GRASP, Institute of Physics B5a, University of Liège, B4000 Liège, Belgium.

Manipulation of floating objects, whether solid or liquid, spanning from microscopic to mesoscopic sizes, is crucial in various microfluidics and microfabrication applications. While capillary menisci naturally self-assemble and transport floating particles, their shapes and sizes are limited by the properties of the fluid and the objects involved. We herein introduce an innovative and versatile method that harnesses the superposition of capillary menisci to curve liquid interfaces without size limit. By using 3D-printed spines piercing the interface, we can finely adjust height gradients across the liquid surface to create any liquid topography at low cost. Thus, our method becomes a powerful tool for manipulating floating objects of all sizes. Combining experimental demonstrations and theoretical modeling, we study the liquid elevation created by specific spine dispositions and the three-dimensional manipulation of submillimetric particles. Multiple examples showcase the method's potential applications, including sorting and capturing particles, which could pave the way for cleaning fluid interfaces.

Under gravity, a liquid maintains a flat profile. However, when in contact with other bodies, whether liquid or solid, or the container walls, it exhibits a characteristic curvature known as the meniscus. This curvature is governed by the delicate interplay between surface tension and gravity and is constrained by the capillary length λ, approximately 2.7 mm for the water-air interface. The occurrence of capillary menisci represents a prevalent phenomenon extensively discussed in physics textbooks [1]. In nature, they serve various purposes. Menisci enhance the aggregation of objects at liquid interfaces, like mosquito eggs [2], bubbles [3], or even cereals [4]. Water-walking insects also utilize menisci to facilitate their motion to reach the shore [5]. The menisci created by surface-piercing vegetation serve to capture particles on water surfaces [6, 7]. All these natural phenomena have inspired scientists to use specific menisci to self-assemble [8–14], transport [15–17], or manipulate [18] floating objects. Curved interfaces have also been proposed to self-assemble and manipulate particles, spherical or anisotropic, into specific structures [18–27]. While for colloidal and submillimetric particles, the curvature only needs to have a short extent, specific aggregations and manipulations of larger floating particles, like bubbles, droplets or solid bodies, requires much larger liquid deformations. Whereas the meniscus extension is limited by λ, when multiple menisci are close together, i.e., with a spacing smaller than λ, all these deformations superimpose. Therefore, we propose herein to superpose numerous menisci, each forming around regularly arranged 3D-printed spines to create any kind of liquid deformation, from specific microfluidics devices to artistic shapes, without limitations in size or extent. Additionally, we prove that the giant and versatile menisci created by this low-cost method can also achieve 3D manipulation of floating particles. We also highlight the wide variety of applications that could benefit from this work, ranging from particle sorting to interface cleaning.

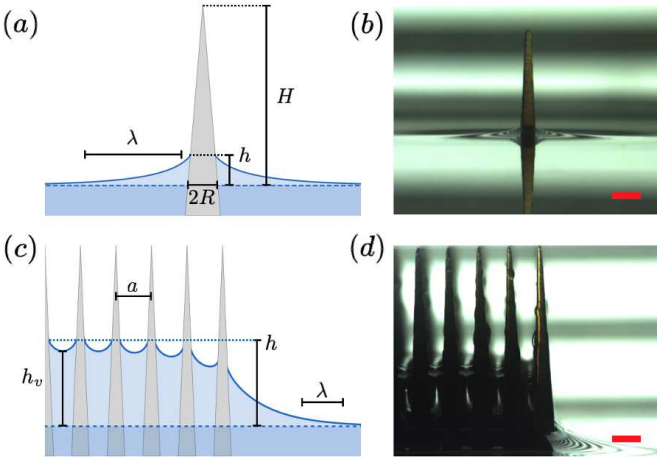

FIG. 1. (a) Sketch of a single conical spine crossing the liquid-air interface. The geometrical characteristics of the spine H and R and the associated meniscus height h are emphasized. The dashed horizontal line denotes the undisturbed interface $z = 0$. (b) Picture of a 3D-printed conical spine illustrating the formation of the meniscus. (c) Sketch of the edge of a square array of spines separated by a. The water profile is shown to highlight the slight undulation of the interface between the spines from a maximal height h to a lower liquid height h_v between spines. (d) A closeup of the liquid menisci at the edge of a square lattice. The liquid interface is 3.5 mm above the undisturbed interface. Scale bars: 1 mm

* Corresponding author: megan.delens@uliege.be

SINGLE SPINE

Let us consider a conical spine crossing the water-air interface. Figure 1(a) presents a sketch of the conical spine defining its geometrical characteristics: the radius R at the undisturbed water level $z = 0$ and the height H. A meniscus is forming around such a spine and its height at the contact line is given by h. Figure 1(b) presents a picture of the typical meniscus forming around a 3D printed spine with a half opening angle $\alpha = \arctan(R/H)$ being $\alpha = 3°$. The shape of the meniscus $z(x, y)$ is determined by the condition that the surface overpressure, which arises from surface tension and is directly related to the curvature of the interface, matches the hydrostatic pressure difference caused by the interface's deformation [1]. In an approach where interface slopes are considered small enough, this condition is mathematically written as the linearized Laplace-Young equation

$$\rho g z = \gamma \nabla^2 z, \tag{1}$$

defining the capillary length

$$\lambda = \sqrt{\frac{\gamma}{\rho g}} \tag{2}$$

which represents the distance over which capillary forces dominate gravitational forces. Several research studies, including those conducted by Lo [28], Kralchevsky [29], and Cooray [30], among others, have been undertaken to investigate the formation of the meniscus around a vertical cylinder. Far from the cylinder or when $R \ll \lambda$, Eq.(1) can be rewritten in cylindrical coordinates thanks to the cylinder's axisymmetry. Its solution gives the profile z as a function of the radial distance r counted from the center of the cylinder. One has

$$z(r) = Q K_0 \left(\frac{r}{\lambda} \right), \tag{3}$$

where K_0 is a decaying zero-order modified Bessel function of the second kind and Q is a constant of integration usually called the *capillary charge* of the cylinder and has a crucial importance for capillary interactions [31]. For a cylinder piercing a liquid-fluid interface, Cooray *et al.* [30] have determined Q by using Archimedes principle stating that, at equilibrium, the weight of the liquid lifted in the meniscus must equal the capillary force acting on the contact line. For the cylinder, this characteristic elevation is $Q_{cyl} = R \cos\theta$, where θ is the contact angle. For the conical spine studied herein, all of the previous assumptions still hold since the contact line keeps axisymmetry. Yet, the contact line radius changes with the liquid height. For the conical spine, we, therefore, assume a characteristic elevation

$$Q = (R - h \tan\alpha) \cos(\theta + \alpha). \tag{4}$$

The above general description (3) of the meniscus tells us that the horizontal extension of the meniscus is limited by the capillary length λ.

REGULARLY ARRANGED SPINES

A major motivation of the present work is to defy this limitation by creating giant menisci with a horizontal extension much larger than λ. In other words, we would like to obtain a steady situation in which the interface is tilted over the entire container size. To reach this challenging situation, we consider an array of identical conical spines. Each spine crossing the interface is the origin of a meniscus, described by Eq.(3). When they are close to each other, i.e., when the lattice spacing $a < \lambda$, the menisci created on neighboring spines superimpose. Regular microstructures are also notably used to mimic the wetting of specific surfaces [32, 33], like porous materials [34, 35] or super-hydrophobic surfaces [36]. Figure 1(c,d) shows a sketch and a picture of the edge of a square lattice of spines. Inside the lattice, the liquid is seen to rise above the undisturbed interface, proving that the effect is quite significant. On average, the interface on the whole lattice is nearly flat. Nevertheless, small valleys are seen in between neighboring spines. In these valleys, the interface height h_v is slightly smaller than h.

Measurements of the interface position have been done by optical means. Figure 2(a) plots the heights h and h_v as a function of unit cell area A for 42 different lattices where the colors distinguish square (blue), triangular (red) and hexagonal lattices (green). All lattices are 3D printed with fixed spine shapes ($R = 0.2$ mm and $\alpha = 1.15°$). The contact angle is fixed by the 3D-printed material and is $\theta = 60°$. Only the lattice spacing a and symmetry were modified (see Materials for fabrication details). In the plot of Figure 2(a), the darker dot represents the highest measurement h at the contact line while the light-colored dot represents the lowest elevation h_v found in between two adjacent spines. For small lattice spacing a, h and h_v are quite similar, while the difference between those couples of points seems to increase with the unit cell area A. One should remark that similar behavior is obtained for all lattice types, whatever their symmetrical features. The relevant parameter is the unit cell area A. A last remark concerns high water elevations h up to 5-6 mm that can be reached with short lattice spacing. This order of magnitude is comparable to the capillary rise in a millimeter tube as given by Jurin's law [37].

To model the liquid elevation within the capillary lattice, we assume that the interface is a linear superposition of all menisci formed around all spines. This superposition approximation is due to Nicolson [3] and is commonly used to estimate the capillary interactions acting between floating bodies [2–4, 12, 14, 29–31, 38–42]. Vassileva and co-workers [42] showed that using the linear superposition principle to estimate the capillary interaction between two cylinders of radius R at distance d is valid when $d > 4R$. Extending this result to our study, we assume the superposition approximation to be valid when $a > 4(R - h \tan\alpha)$. Inside the lattice, the liquid elevation at horizontal position $\vec{r} = (x, y)$ is therefore given

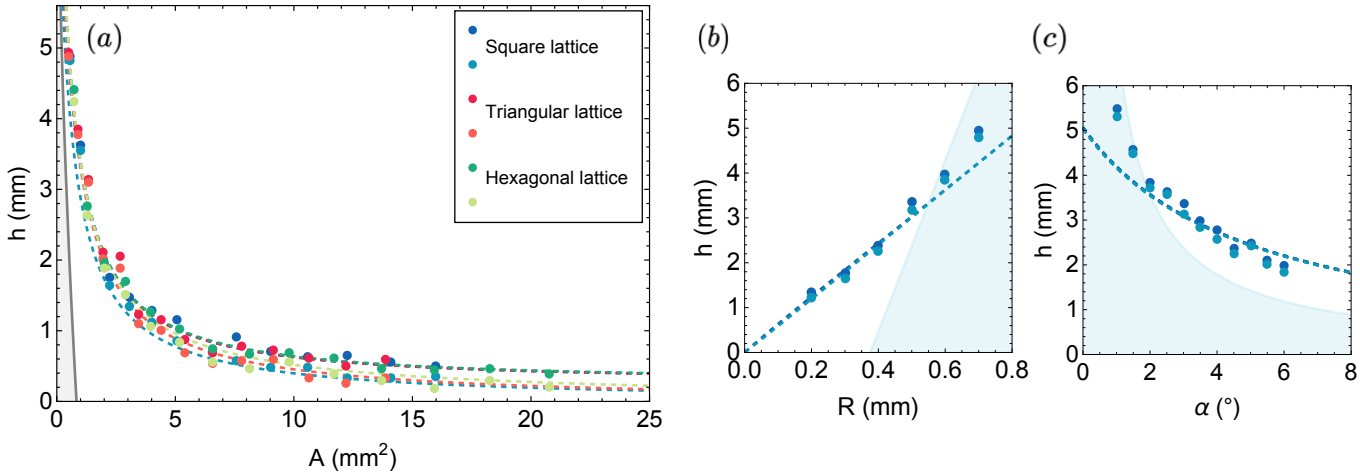

FIG. 2. (a) Measured height at meniscus h and in between spines h_v of water in 42 different lattices as a function of the area of the Voronoi cell. Square, triangular, and hexagonal lattices are illustrated in different colors. Dark colors and light colors are respectively h and h_v measurements. Spines' characteristics are $R = 0.2$ mm and $\alpha = 1.15°$. The dashed curves are predictions of Eq.(6) and (7). The grey region is the region over which the superposition approximation is no longer valid for every lattice symmetry. (b) Elevations h and h_v of the interface in a square lattice as a function of the spine radius R when $\alpha = 3°$ and $A = 2.25$ mm^2. The light-blue area represents the limit of the superposition principle. (c) Height h and h_v as a function of the angle α for spines of radius $R = 0.5$ mm and $A = 2.25$ mm^2.

by

$$z(x,y) = Q\sum_{k,\ell} K_0\left(\frac{|\vec{r}-\vec{r}_{k,\ell}|}{\lambda}\right) = Q\sigma(x,y) \tag{5}$$

where k and ℓ are lattice indices running over the entire structure, with $\vec{r}_{k,\ell} = (ka, \ell a)$ for the square lattice. Looking around the central spine, i.e. when $k = \ell = 0$, and replacing Q by its expression in Eq.(4), one founds the expression of the liquid elevation h at the meniscus:

$$h = z(R,0) = R\left(\frac{1}{\cos(\theta+\alpha)\sigma(R,0)} + \tan(\alpha)\right)^{-1} \tag{6}$$

and the liquid elevation of the valley in between neighboring spines:

$$h_v = z(a/2,0) = (R - h\tan\alpha)\cos(\theta+\alpha)\sigma(a/2,0) \tag{7}$$

The profiles in the sketch of Figure 1(c) were drawn using this model. The equilibrium height of the meniscus around the spines is therefore driven by three main geometrical parameters : (i) the lattice spacing a, (ii) the spine radius R at $z = 0$, and (iii) the opening angle α. One should remark that the physical parameters are the capillary length λ and the contact angle θ which are materials/liquid dependent. The dashed curves in Figure 2(a) represent the h and h_v heights predicted by Eqs.(6) and (7) with the geometrical and wetting properties of the spines. One observes that this simple approach captures remarkably well the behavior of both h and h_v for all lattice spacings. As expected, the difference between h and h_v is getting closer as the lattice spacing decreases, meaning that the liquid inside the lattice is getting more flat. Note that the data and the expressions of h and h_v have been plotted as a function of the unit cell area A to compare the different lattice symmetries easily. For regular arrays, the Voronoi cell area is $A = a^2$ for the square lattice, $A = \sqrt{3}a^2/2$ for the triangular lattice, and $A = 3\sqrt{3}a^2/4$ for the hexagonal lattice. For all lattice symmetry, the grey area in Figure 2(a) represents the limit of the superposition approximation being the region where $a < 4(R - h\tan\alpha)$. One observes that all the experimental data fall within the range of validity of our model.

To modify the liquid height of the interface, one can also adjust other geometrical parameters such as the base radius of the cone R, or the opening angle α. Figure 2(b) presents plots of the experimental measurements of the liquid heights h and h_v in a square lattice when the spine radius R increases keeping $A = 2.25$ mm^2 and $\alpha = 3°$ fixed. The dashed curves represent the h and h_v heights as a function of R predicted by our model. The light blue area represents the region where the superposition principle is no longer considered valid. The experimental data exhibit good agreement with our model outside this region. When the superposition approximation reaches its limit, our model tends to underestimate the liquid elevation, which is consistent with the work of Vasilleva *et al* [42]. Figure 2(c) presents similar measurements for square arrays as a function of α and with other parameters fixed ($R = 0.5$ mm and $A = 2.25$ mm^2). Once again, the model matches well the data within its limit, i.e. for larger angles α. Indeed, the contact line radius must be

small compared to the lattice spacing for the model to be accurate and the contact line radius decreases as α increases.

SPECIFIC LIQUID TOPOGRAPHY

From the above results, we prove that the liquid height can be controlled by the geometrical characteristics A, R, and α, of an array of conical spines. The horizontal expansion of the menisci is no longer limited by the capillary length. Indeed, as the menisci superimpose, the size of the total deformation is only limited by the dimension of the array. Moreover, the geometry of each spine or the lattice spacing can be adjusted for pinning the interface at different heights within a unique array. Having effectively captured the impact of these parameters on the liquid elevation, we can employ this method to program unique liquid topography.

Elementary topographies can be simply programmed by varying, gradually or not, the lattice spacing a or the total height of the spine H along one direction, radially or else. Figure 3 shows various examples to showcase the method's versatility and the wide range of menisci that can be generated. In Figure 3(a) and (b), two tilted interfaces are produced: (a) the first one is by gradually decreasing the total height H, which is equivalent to modifying the radius of the contact line while keeping the other parameters fixed, and (b) the second slope is obtained by increasing the lattice spacing a from left to right. Figures 3(c) and (d) display respectively a parabolic and a sinusoidal liquid interface produced by varying H quadratically and sinusoidally. Conical spines are truncated above the contact line to highlight the liquid interface. Figure 3(e) displays a hemispherical meniscus created by decreasing radially the total height H. Finally, Figure 3(f) shows the meniscus created by two adjacent inclines with perpendicular slopes thus creating a 90° turn in the height gradient. This meniscus is created by decreasing H and keeping R fixed to 0.5 mm.

To program arbitrary and complex liquid topographies, we solve the inverse problem of Eq.(6): starting from the desired liquid height, we calculate the corresponding spines and lattice parameters. This allows us to create any liquid landscape from a given target shape, as exemplified in Figure 4. From the grayscale image of the *Atomium*, the famous Belgian monument, shown in (a), we designed a lattice of truncated conical spines where each spine represents a pixel and of different total height H. The values of H were determined based on the desired liquid elevation h, which is linked to each pixel value ranging from 0 to 255. As the liquid invades the lattice, it rises to different heights, resulting in a three-dimensional representation of the *Atomium*, as shown in Figure 4(b), which offers a perspective view of the experiment. Our method to design the device that creates artistic liquid landscapes from any 2D images or 3D coordinates has been implemented in a Mathematica code which is made available on GitHub (see Code Availability).

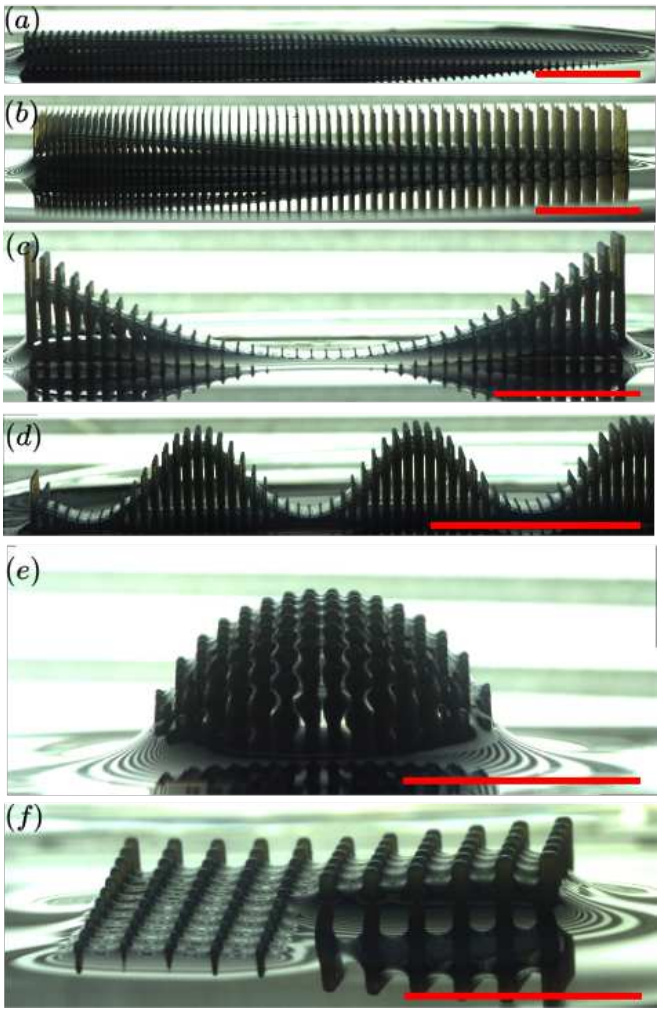

FIG. 3. Various examples of elementary topographies. Scale bars: 10 mm. (a) A liquid incline providing a tilted giant meniscus at equilibrium. The total height H of the spines gradually decreases along the lattice from left to right while the radius $R = 0.2$ mm is constant. (b) The same incline created by another lattice where the lattice spacing a gradually increases from left to right. (c) A quadratic well created by varying quadratically the height H of spines of radius $R = 0.3$ mm. (d) A sine wave topography created by sinusoidally varying the total height H of the spines of radius $R = 0.2$ mm. (e) A hemisphere created by radially decreasing the total height H of spines of the same radius $R = 0.3$ mm. (f) Two adjacent inclines with perpendicular slopes, therefore, creating a 90° turn in the height gradient. The inclines are created by varying the height H of spines of radius $R = 0.5$ mm.

MENISCUS-INDUCED MICROMANIPULATIONS

The broad variety of menisci that can be created by specific arrangements of spines gives direct inspiration for micromanipulation. Indeed, when a particle floats

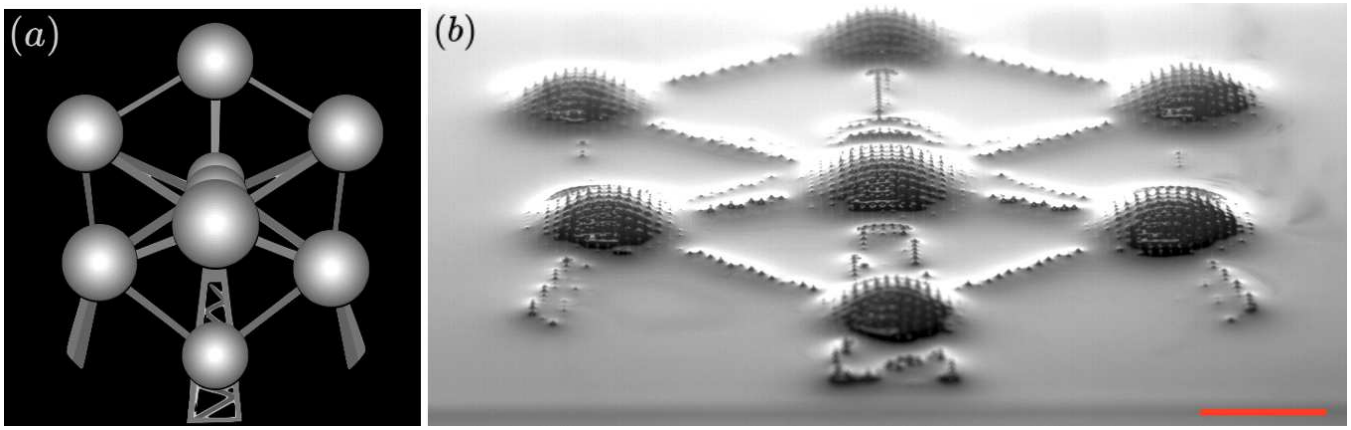

FIG. 4. From this simplified 2D-image of the *Atomium* monument in grey levels (a), a lattice of truncated conical spines has been designed and 3D-printed (b). As the liquid invades the device, it rises to reproduce the *Atomium*. Scale bar: 10 mm.

on a surface that is tilted either by the presence of another particle, a wall meniscus, or, in our case, some spines, the resulting force is no longer perpendicular to the surface, which results in a net movement along the surface. Therefore, light particles, such as bubbles, move upward along the meniscus, following the height gradient, while heavier particles denser than the liquid move downward along the interface slope [3, 4]. This simple assumption, first proposed by Nicolson [3], allows to evaluate the capillary interaction between a particle and another meniscus by computing the gravitational potential energy of the particle at a specific height z in the latter meniscus. Thus, the interaction potential simply takes the shape of the liquid profile $z(x, y)$ in which the particle sits. In 2022, Peng *et al.* have notably achieved directional bubble transport on a few slippery oil-infused pillars with height-gradient [16]. Being aware that complex tridimensional capillary transport can only be achieved by complexifying the liquid topography, we herein propose the use of specific arrays of spines as an effective strategy for particle transport at liquid interfaces.

To test our strategy, we conducted transport experiments of a heavy submillimeter bead floating on desired liquid topographies. As a first experiment, we successfully achieved unidirectional micromanipulation using the array shown in Figure 3(a) forming a giant slope along the interface. Figure 5(a) presents a 3D plot illustrating the $z(x, y)$ profile of the meniscus, calculated using Eq.(5), superimposed on the 3D STL file of the device. This plot effectively illustrates a liquid slope of 4°. The grayscale image within the same figure provides a top-down view of the device, with trajectories of 400 μm diameter beads color-coded according to their instantaneous speed. Similar motions are observed in each row, following the slope of the tilted interface. By varying the particle size, the steepness of the slope, or the lattice spacing, we observed similar behaviors, but at different speeds. For instance, under the same incline, a 500 μm bead is faster than an 800 μm bead which is also faster than a 400μm bead. When testing slope varying from 1° to 5° in increments of 0.5 °, we observe a maximal speed for the slope of 3 ° for all bead sizes. These counter-intuitive observations emphasize the complexity of the forces acting on the beads. The drag force on spherical particles trapped at liquid interfaces depends on various factors, including the shape of the interface, whether the three-phase contact line is pinned or not, the immersion depth, and the driving force [43–46]. In our case, the liquid interface is not only tilted but also slightly undulated following the periodic structure of the array, which highly complicates the bead's dynamics. Therefore, the precise dynamics of particles manipulated in our device will be studied in future works. However, it should be noted that because the particles reach different speeds depending on their size, when the beads leave the device they come to rest at distinct positions. This observation opens up exciting possibilities for sorting particles based on their size or wettability.

More strikingly, the multi-directional transport of particles can also be performed by other liquid topographies. Two examples are shown in Figure 5(b) and (c). Figure 5(b) presents the calculated liquid profile of the array displayed in Figure 3(f) and the trajectory of an 800 μm bead descending the slope. The bead first falls down the slope along the x-direction. When the height gradient in the x-direction vanishes, the bead briefly stops and then continues its descent along the y-direction gradient. The 800 μm stops permanently inside the device when the height gradient and the bead's inertia can no longer overcome the drag force and the slight undulation of the interface. We note that smaller beads (400 μm and 500 μm) came to rest outside this device. Once again, different particles are sorted and the array controls the final positions. In Figure 5(c), we display a particular lattice forming a sinusoidal valley with a slight slope, allowing the bead to make a series of turns while descending the hill. Unlike the constant speed measured on the liquid slope of Figure 5(a), one can observe from

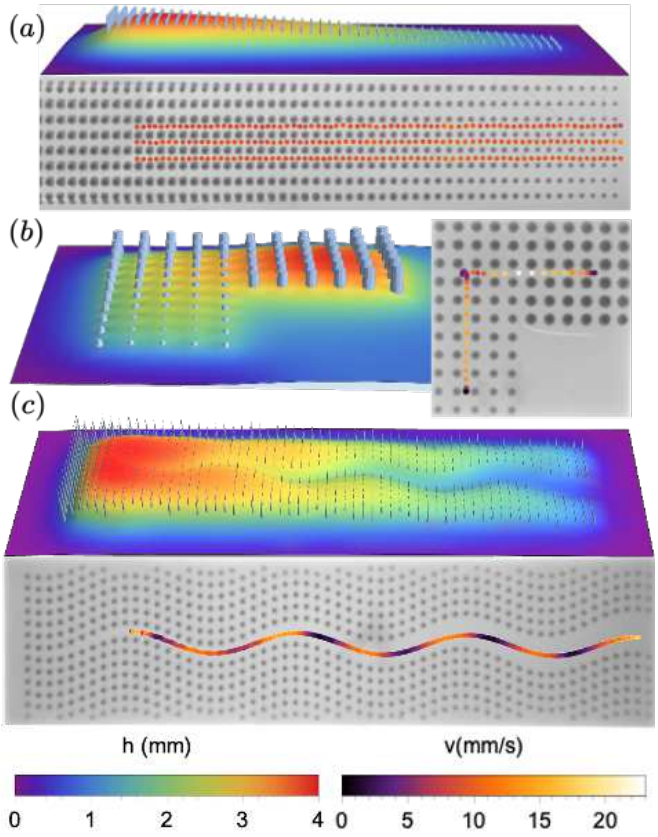

FIG. 5. The 3D plots, calculated using Eq.(5), display the liquid landscape created by an arrangement of spines piercing the liquid. The plot is rainbow-colored according to the liquid elevation and the spines are colored in light blue. In each subfigure, trajectories of heavy submillimeter beads inside the same arrangement are represented and are color-coded according to their speed from purple to yellow.

the color-coded trajectory of a 500 μm bead that it is always decelerated in the turns, i.e., when the direction of motion changes, just as in the 90° turn of Figure 5(b). These illustrating examples offer promising prospects for precise object transport, such as positioning objects beneath a microscope lens, the utilization of liquid curvature as a 'capillary tweezer' [15], or favoring specific structures on capillary self-assemblies, such as the side-by-side assembly of cylindrical particles on a curved interface [19, 20, 23, 27]. It is worth noting that this method of manipulation works for objects of any nature, solid or liquid, as long as they are attached to the liquid interface. Furthermore, as long as the distance between the spines is on the order of the capillary length, even microscopic objects can be controlled [18]. As the total size of the device is unlimited, one major and crucial application of our method could be the cleaning of interfaces from specific oil microdroplets and microscopic objects.

The innovative approach proposed herein utilizes arrays of 3D-printed conical spines to manipulate liquid surfaces in unique ways. By controlling the arrangement, height, and geometry of these spines, we successfully created diverse liquid landscapes, from tilted surfaces to artistic 3D structures. This cost-effective and quick-to-implement method allows for precise micromanipulation of floating particles, exploiting the interaction between particles and menisci. We highlight the potential of our technique for sorting and trapping mesoscopic to microscopic objects but also for cleaning liquid interfaces from microdroplets. While our devices are currently static, the next step could be to actuate each spine to dynamically program the interface curvature. We can imagine spines that can vertically move to change the contact line radius and therefore dynamically change the liquid height h [15]. We might also consider using other types of materials like magnetic [47] and magnetoelastic materials [48] or shape-shifting [33] and shape memory polymers [41] to actuate the capillary meniscus locally.

ACKNOWLEDGMENTS

This work is financially supported by the University of Liège through the CESAM Research Unit. It is also financially supported by the FNRS CDR project number J.0186.23 entitled "Magnetocapillary Interactions for Locomotion at Liquid Interfaces" (MILLI).

AUTHOR CONTRIBUTIONS

All authors have developed the original idea of the array of spines. M.D. and A.F. developed the script for designing the spines. A.F. conducted the experiments. M.D. did the theoretical models. All authors participated in the editing of the manuscript. M.D. and A.F. contributed equally.

COMPETING INTERESTS

The authors declare no competing interests.

METHODS

Design and 3D printing The devices have been designed using a Mathematica script that creates all the spines with specific characteristics and in the desired arrangement with a 2 mm base. The script then exports the 3D graphics in an STL file (See Code Availability). Since the lattice spacing a and the shape of the spines can be modified, about 60 different devices were printed using a PolyJet 3D printer (Stratasys Object Prime 30). The PolyJet method consists of jetting out droplets of resin onto the platform which

are then cured using UV light. It results in an excellent announced resolution of up to 16 μm. We used a resin similar to ABS plastic (Vero Blue) in a glossy finish.

Experimental measurements The lattice was placed in the center of a Petri dish. The amount of water added to the system was controlled to define $z = 0$. The water level has been determined by optical means with a camera taking pictures from the side. The height h of the liquid above the undisturbed interface was measured by image analysis. For the experiments with solid particles, we took videos from above the device and then tracked the particles.

DATA AVAILABILITY

The data supporting the findings of this study are available from the corresponding author upon reasonable request.

CODE AVAILABILITY

The code for creating an arrangement of truncated conical spines that reproduces a gray-scale image is implemented in Mathematica (Version 13.3). This code and CAD files for 3D printing the devices presented in this paper can be found at `https://github.com/GRASP-LAB/3D-printed-spines`.

[1] P.-G. Gennes, F. Brochard-Wyart, D. Quéré, *et al.*, *Capillarity and wetting phenomena: drops, bubbles, pearls, waves* (Springer, 2004).
[2] J. Loudet and B. Pouligny, The European Physical Journal E **34**, 1 (2011).
[3] M. M. Nicolson, Math. Proc. Cambridge Philos. Soc. **45**, 288 (1949).
[4] D. Vella and L. Mahadevan, Am. J. Phys. **73**, 817 (2005).
[5] D. L. Hu and J. W. Bush, Nature **437**, 733 (2005).
[6] P. Peruzzo, A. Defina, and H. Nepf, Water Resources Research **48** (2012).
[7] P. Peruzzo, A. Defina, H. M. Nepf, and R. Stocker, Physical review letters **111**, 164501 (2013).
[8] N. Bowden, A. Terfort, J. Carbeck, and G. M. Whitesides, Science **276**, 233 (1997).
[9] G. M. Whitesides and B. Grzybowski, Science **295**, 2418 (2002).
[10] M. Boncheva and G. M. Whitesides, MRS bulletin **30**, 736 (2005).
[11] J. A. Pelesko, *Self assembly: the science of things that put themselves together* (Chapman and Hall/CRC, 2007).
[12] M. Poty, G. Lumay, and N. Vandewalle, New Journal of Physics **16**, 023013 (2014).
[13] S. Dasgupta, T. Auth, and G. Gompper, Journal of Physics: Condensed Matter **29**, 373003 (2017).
[14] M. Delens, Y. Collard, and N. Vandewalle, Physical Review Fluids **8**, 074001 (2023).
[15] X. Liu, W. Zhou, F. Tang, H. Zheng, and S. W. Joo, Sensors and Actuators B: Chemical **370**, 132380 (2022).
[16] Y. Peng, Y. Jiao, C. Li, S. Zhu, C. Chen, Y. Hu, J. Li, Y. Cao, and D. Wu, Langmuir **38**, 15001 (2022).
[17] J. Jiang, J. Gao, H. Zhang, W. He, J. Zhang, D. Daniel, and X. Yao, Proceedings of the National Academy of Sciences **116**, 2482 (2019).
[18] C. Zeng, M. W. Faaborg, A. Sherif, M. J. Falk, R. Hajian, M. Xiao, K. Hartig, Y. Bar-Sinai, M. P. Brenner, and V. N. Manoharan, Nature **611**, 68 (2022).
[19] E. P. Lewandowski, J. A. Bernate, P. C. Searson, and K. J. Stebe, Langmuir **24**, 9302 (2008), pMID: 18661958, https://doi.org/10.1021/la801167h.
[20] M. Cavallaro Jr, L. Botto, E. P. Lewandowski, M. Wang, and K. J. Stebe, Proceedings of the National Academy of Sciences **108**, 20923 (2011).
[21] L. Botto, E. P. Lewandowski, M. Cavallaro, and K. J. Stebe, Soft Matter **8**, 9957 (2012).
[22] N. Vandewalle, L. Clermont, D. Terwagne, S. Dorbolo, E. Mersch, and G. Lumay, Physical Review E **85**, 041402 (2012).
[23] C. Zeng, F. Brau, B. Davidovitch, and A. D. Dinsmore, Soft Matter **8**, 8582 (2012).
[24] I. B. Liu, M. A. Gharbi, V. L. Ngo, R. D. Kamien, S. Yang, and K. J. Stebe, Proceedings of the National Academy of Sciences **112**, 6336 (2015).
[25] T. V. Vinay, T. N. Banuprasad, S. D. George, S. Varghese, and S. N. Varanakkottu, Advanced Materials Interfaces **4**, 1601231 (2017).
[26] G. Xie, P. Li, P. Y. Kim, P.-Y. Gu, B. A. Helms, P. D. Ashby, L. Jiang, and T. P. Russell, Nature Chemistry **14**, 208 (2022).
[27] J. L. Eatson, J. R. Gordon, P. Cegielski, A. L. Giesecke, S. Suckow, A. Rao, O. F. Silvestre, L. M. Liz-Marzn, T. S. Horozov, and D. M. A. Buzza, Langmuir **39**, 6006 (2023), pMID: 37071832, https://doi.org/10.1021/acs.langmuir.3c00016.
[28] L. L. Lo, Journal of Fluid Mechanics **132**, 65 (1983).
[29] P. Kralchevsky, V. Paunov, N. Denkov, I. Ivanov, and K. Nagayama, Journal of colloid and interface science **155**, 420 (1993).
[30] H. Cooray, P. Cicuta, and D. Vella, Journal of Physics: Condensed Matter **24**, 284104 (2012).
[31] V. Paunov, P. Kralchevsky, N. Denkov, and K. Nagayama, Journal of colloid and interface science **157**, 100 (1993).
[32] C. Semprebon, P. Forsberg, C. Priest, and M. Brinkmann, Soft Matter **10**, 5739 (2014).
[33] J. Cappello, B. Scheid, F. Brau, and E. Siéfert, Proceedings of the National Academy of Sciences **120**, e2216001120 (2023).
[34] J. Bico, U. Thiele, and D. Quéré, Colloids and Surfaces A: Physicochemical and Engineering Aspects **206**, 41 (2002).
[35] D. Quéré, Annu. Rev. Mater. Res. **38**, 71 (2008).
[36] Y. Yang, X. Li, X. Zheng, Z. Chen, Q. Zhou, and Y. Chen, Advanced materials **30**, 1704912 (2018).
[37] J. Jurin, Philosophical Transactions of the Royal Society of London **30**, 739 (1717).

[38] P. A. Kralchevsky and K. Nagayama, Langmuir **10**, 23 (1994).
[39] D. Chan, J. Henry Jr, and L. White, Journal of Colloid and Interface Science **79**, 410 (1981).
[40] J.-C. Loudet, A. M. Alsayed, J. Zhang, and A. G. Yodh, Physical review letters **94**, 018301 (2005).
[41] N. Vandewalle, M. Poty, N. Vanesse, J. Caprasse, T. Defize, and C. Jérôme, Soft Matter **16**, 10320 (2020).
[42] N. D. Vassileva, D. van den Ende, F. Mugele, and J. Mellema, Langmuir **21**, 11190 (2005).
[43] A. Dörr and S. Hardt, Journal of Fluid Mechanics **770**, 5 (2015).
[44] A. Dörr, S. Hardt, H. Masoud, and H. A. Stone, Journal of Fluid Mechanics **790**, 607 (2016).
[45] Z. Zhou, P. M. Vlahovska, and M. J. Miksis, Physical Review Fluids **7**, 124001 (2022).
[46] R. Hunt, Z. Zhao, E. Silver, J. Yan, Y. Bazilevs, and D. M. Harris, Phys. Rev. Fluids **8**, 084003 (2023).
[47] Y. Sun, H. Zhang, Y. Zhao, J. Wu, Y. Zhu, M. Li, and L. Wang, Advanced Materials Technologies , 2300773.
[48] M. Poty, F. Weyer, G. Grosjean, G. Lumay, and N. Vandewalle, The European Physical Journal E **40**, 1 (2017).